Distributed Adaptive Synchronization for Multiple Spacecraft Formation Flying Around Lagrange Point Orbits

Wei Wang[1], Giovanni Mengali[2], Alessandro A. Quarta[2], Jianping Yuan[1]*

[1] *National Key Laboratory of Aerospace Flight Dynamics, Northwestern Polytechnical University, 710072 Xi'an, People's Republic of China*

[2] *Department of Civil and Industrial Engineering, University of Pisa, I-56122 Pisa, Italy*

Abstract

This paper presents a distributed adaptive control framework for multiple spacecraft formation flying around Lagrange point orbits, which account for unmeasurable velocities and (spacecraft) mass uncertainties. The nominal trajectory for the formation system is a halo orbit parameterized by Fourier series expansions. Such an explicit, albeit approximate, description of the nominal trajectory facilitates each spacecraft in formation to include the relative state information into a cooperative feedback control system design, so that the relative motion can be driven towards a desired trajectory while maintaining a group synchronization during the maneuver. The developed distributed control strategies rely on the protocols formulated on an undirected topology with mutual information interactions, utilizing every available neighbor-to-neighbor communication data couplings, in order to improve the reliability of the formation. Numerical simulations show that the proposed adaptive control laws guarantee global asymptotic convergence and system robustness.

Keywords: Formation flying, Halo orbit, Distributed control, Adaptive synchronization

Nomenclature

$a_k^c, a_k^s, b_k^c, b_k^s, c_k^c, c_k^s$	=	k-th order coefficients of Fourier series
$\boldsymbol{e}$	=	relative position errors $[\,\mathrm{km}\,]$
$\mathcal{E}$	=	set of edges
$\boldsymbol{f}$	=	control force, $[N]$
$\mathbb{G}$	=	adjacency matrix (with entries $[g_{ij}]$)
$\mathcal{G}$	=	communication topology graph
$\mathbb{I}$	=	identity matrix
$\mathbb{L}$	=	Laplacian matrix (with entries $[l_{ij}]$)
m	=	mass, $[\,\mathrm{kg}\,]$
N	=	number of spacecraft
n	=	order of Fourier series
n_r	=	angular velocity of relative orbit, $[\,\mathrm{rad/day}\,]$
$\mathbb{O}$	=	zero matrix
O	=	reference frame origin
$\boldsymbol{r}$	=	position vector (with $r = \|\boldsymbol{r}\|$), $[\,\mathrm{au}\,]$
S	=	spacecraft

*Corresponding author

Email addresses: 418362467@qq.com (Wei Wang[1]), g.mengali@ing.unipi.it (Giovanni Mengali[2]), a.quarta@ing.unipi.it (Alessandro A. Quarta[2]), jyuan@nwpu.edu.cn (Jianping Yuan[1])

t	=	time, [days]
T	=	period of nominal halo orbit, [days]
$\mathcal{T}$	=	rotating reference frame
$\boldsymbol{u}$	=	propulsive (control) acceleration, [m/s^2]
$\mathcal{V}$	=	set of vertices
$x,\, y,\, z$	=	components of position vector in rotating frame
$\hat{\boldsymbol{x}},\, \hat{\boldsymbol{y}},\, \hat{\boldsymbol{z}}$	=	unit vectors of rotating coordinate axes
$\boldsymbol{X}$	=	state vector (with $\boldsymbol{X} \triangleq [\boldsymbol{r}^{\mathrm{T}}, \dot{\boldsymbol{r}}^{\mathrm{T}}]^{\mathrm{T}}$)
Δv	=	velocity change, [m/s]
$\boldsymbol{\Phi}$	=	state-transition matrix
μ	=	normalized Earth mass
$\rho_x,\, \rho_y,\, \rho_z$	=	components of relative position vector, [km]
$\boldsymbol{\rho}$	=	relative position vector with respect to nominal orbit, [km]
υ	=	vertex
$\boldsymbol{\omega}$	=	angular velocity vector of rotating frame (with $\omega = \|\boldsymbol{\omega}\|$), [rad/day]

Subscripts

0	=	initial value
ES	=	Earth-spacecraft
f	=	final value
h	=	halo orbit
i	=	i-th spacecraft
SS	=	Sun-spacecraft

Superscripts

T	=	transpose
$\star$	=	desired value
$\cdot$	=	time derivative
$\wedge$	=	unit vector
$\sim$	=	estimated value

1. Introduction

Formation flying enables multiple vehicles to operate closely to accomplish complex space tasks that would be difficult to obtain with a single, conventional, spacecraft. Exploiting a task distribution among smaller, less-expensive vehicles, the spacecraft in a formation are able to share information and operate cooperatively, thus enhancing the system flexibility and reducing the overall mission costs [1]. Besides, formation flying also provides a means to improve specialized functions, such as image resolution and in-situ observation in astronomical missions [2]. Due to its distinctive peculiarity, some advanced formation flying-based mission scenarios have been proposed in the last decades in both geocentric and deep space environment. In this context, interesting examples are offered by PRISMA [3], a demonstration mission for autonomous technologies and on-orbit-servicing techniques, and Darwin [4], a scientific mission for Earth-like exo-planet detections.

One of the most practical applications of the formation flying concept is to observe (or explore) the celestial bodies by placing a number of spacecraft around the Lagrange points, known as the five equilibrium (stationary) solutions to the circular restricted three-body problem (CR3BP) [5]. A peculiarity of missions carried out near the natural (or artificial [6, 7, 8]) Lagrange points is that the formation may operate with an unobstructed view and is rarely affected by planetary perturbations (e.g. atmospheric and geomagnetic forces). For example, in the Sun-Earth system, the halo (or Lissajous) orbits in the vicinity of L_2 point naturally avoid the Sun eclipse, and are therefore suitable for measuring the cosmic microwave background.

Also, orbits around L_1 point are never shadowed by Earth, and always view its sunlit hemisphere. Therefore, they usually serve as an interplanetary early warning storm monitor for solar disturbances. [9]

Even though formation flying around Lagrange point orbits provides such valuable features as low-cost replacement of a faulty agent, it also poses a great challenge. In fact, since orbits around the collinear points are inherently unstable, a continuous active control is necessary to achieve long-term bounded relative motion. To that end, a number of formation control algorithms have been discussed, which can be roughly categorized into tight [10, 11, 12, 13] and loose [14, 15, 16] strategies. The tight control method consists in stabilizing the spacecraft relative motion with respect to a specified nominal trajectory, using Lyapunov or eigenvalue stability theorem. The loose control concept, instead, relies on invariant manifolds theory, using the fact that the relative motion evolves and is always restricted within a bounded region provided some natural low-drift regions are found.

Thus far, much effort has been devoted to the study of formation flying around Lagrange point orbits, however several existing problems yet need to be solved. First, the non-integrability nature of the CR3BP prevents from any analytical representation of a nominal trajectory. Although some closed-form solutions have been discussed in the literature, however, they rely on a linearization procedure or on perturbation expansion-based approximations [5, 17]. The linearized solution is well suited only for small-distances (relative to the Lagrange points), whereas the typical example of an algebraic solution is the well-known third-order approximation discussed by Richardson [17], which however leads to a remarkable deviation from the nominal orbit after about one half period only. In addition, previous studies [18, 19] on formation keeping algorithms around Lagrange point orbits assume the neighboring spacecraft velocity and its mass to be precisely known, which is usually a demanding task for an onboard measuring system. To reduce the operating costs and the spacecraft weight, the problem of guaranteeing the system stability even in the presence of velocity or mass uncertainties becomes crucial, especially when faults or high noises reduce the effectiveness of the on-board sensors. Finally, most of the existing works [10, 11, 12, 13, 19, 20] on this issue are limited to a leader-follower formation structure, rendering an inherent weakness that the leader is a single point of failure for the whole system. To mitigate these risks, the system robustness and its overall redundancy need to be strengthened.

Recognizing these open issues, a distributed framework of multiple spacecraft formation flying around Lagrange point orbits is here discussed. The contributions of this paper are twofold. First, the nominal trajectory is parameterized via high-order Fourier series expansions. Unlike the classical third-order solution that suffers from a huge amount of algebraic manipulations, the Fourier series-based solution relies on a least-square approach and provides a better accuracy as the order of the expansion series increases. Note that the Fourier series-based approach has been recently [21] used to continuate the spacecraft orbit, for long term, in the real Solar System model. Compared to the existing works, the approximate closed-form description of the nominal trajectory captures most nonlinearity. This results in a propellant reduction necessary to maintain the formation around the nominal trajectory. Second, two distributed adaptive synchronization control strategies are proposed to account for unmeasurable spacecraft velocities and mass uncertainties. By exploiting the available information exchange among the formation, every spacecraft updates its state using the data flow transmitted from its local neighbours (not necessarily limited to the nearest one, as is discussed in Ref. [22]), so that the overall redundancy and group robustness are enhanced. Besides, the proposed consensus-based control law also guarantees a time-balanced (synchronization), as well as a high tracking accuracy.

This paper is organized as follows. Section 2 illustrates the mathematical model in the Sun-Earth CR3BP, and presents an approximate analytical solution to the nominal orbit via Fourier series expansions. Section 3 provides two distributed control strategies using mutual information couplings to account for unmeasurable velocities and mass uncertainties, respectively. The control effectiveness is then investigated in Section 4 by means of some numerical simulations. Finally, some concluding remarks are given in Section 5.

2. Problem formulation

In this section, the Sun and Earth are considered as the two primary bodies, and the halo orbit around L_2 point is designated as the nominal trajectory. To describe the relative motion equation of the formation system, it is useful to introduce first the mathematical model used in CR3BP.

2.1. Equations of motion

The dynamic model describing the Sun-Earth CR3BP is formulated in a classical rotating coordinate system $\mathcal{T}(O; \hat{\boldsymbol{x}}, \hat{\boldsymbol{y}}, \hat{\boldsymbol{z}})$, see Fig. 1. The origin O of the reference frame is centered at the system barycenter, while the plane $(\hat{\boldsymbol{x}}, \hat{\boldsymbol{y}})$ coincides with the ecliptic plane, $\hat{\boldsymbol{x}}$ axis points to the Earth and $\hat{\boldsymbol{z}}$ axis is positive in the direction of the angular velocity vector $\boldsymbol{\omega}$. For convenience, a normalized set of units is introduced, such that the total mass of the primaries, the Sun-Earth distance, and the universal gravitation constant are all equal to unity. Accordingly, the period of one Earth-Sun revolution is 2π, and the (normalized) Earth's mass is $\mu = 3.05425 \times 10^{-6}$.

Let $\boldsymbol{r}_i \triangleq [x_i, y_i, z_i]^{\mathrm{T}}$ be the position vector of the generic spacecraft S_i, see Fig. 1. The spacecraft equations of motion in the CR3BP without control input (i.e. without propulsive acceleration), are

$$\ddot{x}_i - 2\dot{y}_i = \frac{\partial\Omega_i}{\partial x_i} \quad , \quad \ddot{y}_i + 2\dot{x}_i = \frac{\partial\Omega_i}{\partial y_i} \quad , \quad \ddot{z}_i = \frac{\partial\Omega_i}{\partial z_i} \tag{1}$$

with

$$\Omega_i \triangleq \frac{x_i^2 + y_i^2}{2} + \frac{1-\mu}{r_{SS_i}} + \frac{\mu}{r_{ES_i}} \tag{2}$$

where the Sun-spacecraft (r_{SS_i}) and Earth-spacecraft (r_{ES_i}) distances are given by

$$r_{SS_i} = \sqrt{(x_i + \mu)^2 + y_i^2 + z_i^2} \tag{3}$$

$$r_{ES_i} = \sqrt{(x_i + \mu - 1)^2 + y_i^2 + z_i^2} \tag{4}$$

For a system described by Eq. (1), there are five natural equilibrium points L_i (with $i = 1, 2, \ldots, 5$), among which the collinear Lagrange points (L_1, L_2, and L_3) are inherently unstable, whereas the triangular Lagrange points (L_4 and L_5) are stable. In particular, halo (or Lissajous) orbits around L_1 and L_2 points are very useful for space-borne observatories. For illustrative purposes, the halo orbit in the neighborhood of L_2 point is here chosen as the nominal trajectory for the spacecraft formation system.

2.2. Nominal trajectory generation

To precisely maintain a spacecraft formation around a halo orbit in the neighborhood of L_2 point, a continuous active control system is required. Most existing studies about this problem use a nominal trajectory [12] based on the linearized form of Eq. (1), or a third-order approximate solution with the aid of the Lindstedt-Poincaré perturbation method [13]. However, none of them is able to provide a good estimation of the actual trajectory, especially for large-size trajectories or long-term propagation. As a consequence, an additional amount of propellant consumption is usually necessary to compensate for the orbital frequency offset in these solutions, because the misestimation in frequency leads to both position and velocity deviations with respect to the natural (reference) trajectory. To provide a satisfactory evaluation of the nominal trajectory, a Fourier series-based solution with a least-square technique is now introduced.

To begin, a differential correction method is used to identify the nominal halo orbit. Let $\boldsymbol{X} \triangleq [\boldsymbol{r}^{\mathrm{T}}, \dot{\boldsymbol{r}}^{\mathrm{T}}]^{\mathrm{T}} = [x, y, z, \dot{x}, \dot{y}, \dot{z}]^{\mathrm{T}}$ be the spacecraft state vector along the trajectory. The state space form of the (variational) equations of motion, relative to the nominal trajectory given by Eq. (1), can be written as

$$\delta\dot{\boldsymbol{X}} = \mathbb{A}\,\delta\boldsymbol{X} \tag{5}$$

where $\delta\boldsymbol{X} \triangleq \boldsymbol{X} - \boldsymbol{X}_h = [\delta x, \delta y, \delta z, \delta\dot{x}, \delta\dot{y}, \delta\dot{z}]^{\mathrm{T}}$ is the spacecraft state variation, and $\mathbb{A}$ is a time-dependent matrix defined as

$$\mathbb{A} \triangleq \begin{bmatrix} \mathbb{O}_3 & \mathbb{I}_3 \\ \mathbb{B} & -\mathbb{C} \end{bmatrix} \tag{6}$$

where $\mathbb{O}_3$ (or $\mathbb{I}_3$) is a 3×3 zero (or identity) matrix. In Eq. (6), the sub-matrices $\mathbb{B}$ and $\mathbb{C}$ are given by

$$\mathbb{B} = \begin{bmatrix} \dfrac{\partial^2\Omega}{\partial x^2} & \dfrac{\partial^2\Omega}{\partial x\,\partial y} & \dfrac{\partial^2\Omega}{\partial x\,\partial z} \\[2mm] \dfrac{\partial^2\Omega}{\partial y\,\partial x} & \dfrac{\partial^2\Omega}{\partial y^2} & \dfrac{\partial^2\Omega}{\partial y\,\partial z} \\[2mm] \dfrac{\partial^2\Omega}{\partial z\,\partial x} & \dfrac{\partial^2\Omega}{\partial z\,\partial y} & \dfrac{\partial^2\Omega}{\partial z^2} \end{bmatrix} \quad , \quad \mathbb{C} = \begin{bmatrix} 0 & -2 & 0 \\ 2 & 0 & 0 \\ 0 & 0 & 0 \end{bmatrix} \tag{7}$$

Equation (5) has a general solution in the form

$$\delta \boldsymbol{X} = \boldsymbol{\Phi}\left(t, t_0\right) \delta \boldsymbol{X}_0 \tag{8}$$

where $\delta \boldsymbol{X}_0$ is the initial (i.e. at time $t_0 \triangleq 0$) value of the vector $\delta \boldsymbol{X}$, and $\boldsymbol{\Phi}\left(t, t_0\right)$ is the state-transition matrix that satisfies

$$\dot{\boldsymbol{\Phi}}\left(t, t_0\right) = \mathbb{A}\,\boldsymbol{\Phi}\left(t, t_0\right) \tag{9}$$

Bearing in mind the initial condition $\boldsymbol{\Phi}\left(t_0, t_0\right) = \mathbb{I}_6$, where $\mathbb{I}_6$ is a 6×6 identity matrix, the state-transition matrix can be numerically solved. Note that the halo orbit is symmetric with respect to the $(\hat{\boldsymbol{x}}, \hat{\boldsymbol{z}})$ plane, therefore only three variables need to be corrected, and $\{\dot{x}, \dot{z}\} = 0$ when the motion trajectory crosses the $(\hat{\boldsymbol{x}}, \hat{\boldsymbol{z}})$ plane. With reference to the classic third-order solution [17] for a favorable initial guess $\boldsymbol{X}_0 = [x_0, 0, z_0, 0, \dot{y}_0, 0]^{\mathrm{T}}$, and integrating Eq. (1) until the trajectory reaches (again) the $(\hat{\boldsymbol{x}}, \hat{\boldsymbol{z}})$ plane, the state vector has a form $\boldsymbol{X}_f^\star = [x_0^\star, 0, z_0^\star, 0, \dot{y}_0^\star, 0]^{\mathrm{T}}$. Let $\delta \boldsymbol{X}_f \triangleq \boldsymbol{X}_f - \boldsymbol{X}_f^\star$ denote the state deviation at one half period and, from Eq. (8), the initial state to be corrected within one iteration is calculated as $\delta \boldsymbol{X}_0 = \boldsymbol{\Phi}^{-1}\left(t_f, t_0\right) \delta \boldsymbol{X}_f$. After several iterative processes, the halo orbit can be obtained with an accuracy of 10^{-10}, that is, with $\{\dot{x}_f^\star, \dot{z}_f^\star\} \le 10^{-10}$.

Although a numerical differential correction method can be implemented to obtain the halo orbit, the design of the formation control system requires an explicit orbit description. To that end, according to Ref. [19], a Fourier series expansion is introduced here with the aim of expressing the nominal orbit in an approximate analytical form as

$$x_h = a_0 + \sum_{k=1}^{n}\left[a_k^c\,\cos\left(k\,\omega\,t\right) + a_k^s\,\sin\left(k\,\omega\,t\right)\right] \tag{10}$$

$$y_h = b_0 + \sum_{k=1}^{n}\left[b_k^c\,\cos\left(k\,\omega\,t\right) + b_k^s\,\sin\left(k\,\omega\,t\right)\right] \tag{11}$$

$$z_h = c_0 + \sum_{k=1}^{n}\left[c_k^c\,\cos\left(k\,\omega\,t\right) + c_k^s\,\sin\left(k\,\omega\,t\right)\right] \tag{12}$$

Retaining Eqs. (10)–(12) to a given order n, the optimal value of the unknown parameters $\boldsymbol{\ell}^\star \triangleq [a_0, a_k^c, a_k^s, b_0, b_k^c, b_k^s, c_0, c_k^c, c_k^s]^{\mathrm{T}}$ can be found by using an unconstrained least-square process, with the minimization index defined as

$$\boldsymbol{\ell}^\star = \arg\min \int_0^T \|\boldsymbol{X} - \boldsymbol{X}_h\|^2 \,\mathrm{d}t \tag{13}$$

where $T = 2\,\pi/\omega$ is the period of the halo orbit.

For example, a nominal halo orbit parameterized via an 8th-order Fourier series approximation is illustrated in Fig. 2, with a period $T = 180.36$ days (i.e. $\omega = 2.02508$) and a Jacobi integral $\mathcal{J} = 3.001$. The coefficients in Eqs. (10)–(12) are listed in Tab. 1. In particular, the (optimal) unknown parameters are found in least-squares sense using standard routines for nonlinear curve-fitting as, for example, the MATLAB function "lsqcurvefit". In order to speed up the iteration convergence, the solver requires an initial guess of the parameters, which can be provided using the procedure described in the appendix of Ref. [17]. Recently, a similar approach has been used also in Ref. [19].

Let $\Delta \tilde{r} \triangleq \|\boldsymbol{r} - \boldsymbol{r}_h\| / \|\boldsymbol{r}\|$ denote the distance error of the approximation, where $\boldsymbol{r}$ is the exact (numerical) position vector of the spacecraft. As is illustrated in Fig. 3, in which the halo orbit is propagated for one period (with $T = 180.36$ days), the 8th-order Fourier series-based solution has a maximum error less than 10^{-7}, which proves a good approximation. In the next section, such an analytical solution will serve both as a basis to address the problem of multiple spacecraft formation flying around a halo orbit, and to facilitate the design of the distributed synchronization control system.

3. Distributed adaptive formation control

The distributed adaptive control algorithms that account for spacecraft velocity and mass uncertainties are now developed for a formation structure with $N \ge 3$ spacecraft, based on a local neighbor-to-neighbor

information. In particular, the communication topology of the relative motion is represented by an undirected topology graph, under the assumption that the information exchange is bidirectional.

To proceed, it is useful to briefly summarize a few concepts from graph theory [23]. An undirected graph $\mathcal{G}$ consists of a finite non-empty vertex set $\mathcal{V} = \{v_1, \ldots, v_N\}$, an edge set $\mathcal{E} = \{(v_1, v_2), \ldots, (v_{N-1}, v_N)\} \subseteq \mathcal{V} \times \mathcal{V}$, and an adjacency matrix $\mathbb{G} \in \mathbb{R}^{N \times N}$. The matrix $\mathbb{G}$ is defined in such a way that its generic entry is $g_{ij} = g_{ji} = 1$ if $(v_i, v_j) \in \mathcal{E}$ with $i \neq j$, whereas $g_{ii} = 0$. Note that $\mathbb{G}$ is symmetric, and $g_{ij} = 0$ if $(v_i, v_j) \notin \mathcal{E}$. The Laplacian matrix $\mathbb{L} = [l_{ij}] \in \mathbb{R}^{N \times N}$ associated with $\mathbb{G}$ is defined as $l_{ij} = -g_{ij}$ and $l_{ii} = \sum\limits_{j=1}^{N} g_{ij}, \forall\, i \neq j$. The matrix $\mathbb{L}$ is symmetric positive semi-definite and $\sum\limits_{j=1}^{N} l_{ij} = 0, \forall\, i \neq j$. A graph is termed connected if there exists a path from every vertex to every other vertex.

In the following analysis, emphasis is given to the case where the information exchange topology is fixed. While modeling the communication topology of the formation system, each spacecraft S_i (with $i = 1, 2, \ldots, N$) is characterized by a vertex, while the exchanged information data between any pair of vertices is represented by an edge. In particular, each spacecraft S_i is assumed to have access to the nominal halo orbit, whose Fourier series-based approximate solution is given by Eqs. (10)–(12).

Keeping multiple spacecraft in a formation around the collinear L_2 point requires continuous active controls, that is, a continuous propulsive acceleration. It is assumed throughout the paper that each spacecraft in formation is equipped with a low-thrust electric propulsion system. Denoting with $\boldsymbol{f}_i \triangleq [f_{xi}, f_{yi}, f_{zi}]^{\mathrm{T}}$ the control thrust and m_i the mass of S_i, Eqs. (1)–(2) become

$$\ddot{\boldsymbol{r}}_i + \mathbb{C}\,\dot{\boldsymbol{r}}_i + \boldsymbol{d}_i = \boldsymbol{f}_i/m_i \tag{14}$$

where matrix $\mathbb{C}$ is given by Eq. (7), and $\boldsymbol{d}_i$ is a vector defined as

$$\boldsymbol{d}_i \triangleq \begin{bmatrix} \dfrac{(1-\mu)\,(x_i+\mu)}{r_{SS_i}^3} + \dfrac{\mu\,(x_i+\mu-1)}{r_{ES_i}^3} - x_i \\ \dfrac{(1-\mu)\,y_i}{r_{SS_i}^3} + \dfrac{\mu\,y_i}{r_{ES_i}^3} - y_i \\ \dfrac{(1-\mu)\,z_i}{r_{SS_i}^3} + \dfrac{\mu\,z_i}{r_{ES_i}^3} \end{bmatrix} \tag{15}$$

The distributed coordination control laws formulated on Eq. (14) is designed in such a way that each spacecraft in the formation tracks the desired trajectory, while maintaining synchronization during the maneuver. Let $\boldsymbol{r}_i^\star$ and $\dot{\boldsymbol{r}}_i^\star$ denote the desired position and velocity of S_i, respectively, and introduce the position error $\boldsymbol{e}_i \triangleq \boldsymbol{r}_i - \boldsymbol{r}_i^\star$, and the velocity error $\dot{\boldsymbol{e}}_i \triangleq \dot{\boldsymbol{r}}_i - \dot{\boldsymbol{r}}_i^\star$. The goal of the consensus-based controller is to solve the distributed formation tracking problem and to achieve a time-balanced transition, i.e. $\boldsymbol{e}_i \to \boldsymbol{e}_j \to \boldsymbol{0}$ and $\dot{\boldsymbol{e}}_i \to \dot{\boldsymbol{e}}_j \to \boldsymbol{0}$.

In the following analysis, two typical cases will be discussed in detail, where the distributed adaptive formation control schemes are developed to account for unmeasurable velocities and mass uncertainties, respectively.

3.1. Adaptive synchronization without velocity measurement

Since velocity measurements are usually less accurate and more expensive than position measurements, it is meaningful to first analyze a case in which the velocity information of the neighboring spacecraft is not available. Accordingly, a passive filter is introduced into the feedback control law to remove the need for

the neighbors' velocity [24], viz.

$$\dot{\boldsymbol{\xi}}_i = \boldsymbol{\Psi}\,\boldsymbol{\xi}_i + \lambda_i^v\,\boldsymbol{e}_i + \kappa \sum_{j=1}^{N} g_{ij}\,(\boldsymbol{e}_i - \boldsymbol{e}_j) \tag{16}$$

$$\boldsymbol{\zeta}_i = \boldsymbol{\Gamma}\left[\boldsymbol{\Psi}\,\boldsymbol{\xi}_i + \lambda_i^v\,\boldsymbol{e}_i + \kappa \sum_{j=1}^{N} g_{ij}\,(\boldsymbol{e}_i - \boldsymbol{e}_j) \right] \tag{17}$$

$$\boldsymbol{f}_i = m_i\left[\ddot{\boldsymbol{r}}_i^\star + \mathbb{C}\,\dot{\boldsymbol{r}}_i^\star + \boldsymbol{d}_i - \lambda_i^p\,\boldsymbol{e}_i - \sum_{j=1}^{N} g_{ij}\,(\boldsymbol{e}_i - \boldsymbol{e}_j) - \boldsymbol{\zeta}_i \right] \tag{18}$$

where $\{\lambda_i^p,\,\lambda_i^v,\,\kappa\} \in \mathbb{R}^+$, $\{\boldsymbol{\xi}_i,\,\boldsymbol{\zeta}_i\} \in \mathbb{R}^3$, $\boldsymbol{\Psi}$ is a Hurwitz matrix, $\boldsymbol{\Gamma} = \boldsymbol{\Gamma}^{\mathrm{T}} \in \mathbb{R}^{3\times3}$ is the positive-definite solution to the Lyapunov equation $\boldsymbol{\Psi}^{\mathrm{T}}\boldsymbol{\Gamma} + \boldsymbol{\Gamma}\,\boldsymbol{\Psi} = -\boldsymbol{\Theta}$, with $\boldsymbol{\Theta} = \boldsymbol{\Theta}^{\mathrm{T}}$ is positive-definite. Note that λ_i^p, λ_i^v, κ, $\boldsymbol{\Psi}$, and $\boldsymbol{\Gamma}$ are all control parameters that must be selected with a trial and error procedure, as is discussed in the succeeding case study. Also recall that no velocity terms of the neighboring spacecraft are involved.

Theorem 1: Using the adaptive control law of Eqs. (16)–(18) for the system represented by Eq. (14), synchronized formation tracking is achieved, that is, $\boldsymbol{e}_i \to \boldsymbol{e}_j \to \boldsymbol{0}$ and $\dot{\boldsymbol{e}}_i \to \dot{\boldsymbol{e}}_j \to \boldsymbol{0}$ as $t \to +\infty$.

Proof: Consider the candidate Lyapunov function

$$V = \frac{1}{2}\sum_{i=1}^{N} \lambda_i^p\,\boldsymbol{e}_i^{\mathrm{T}}\,\boldsymbol{e}_i + \frac{1}{2}\sum_{i=1}^{N} \dot{\boldsymbol{e}}_i^{\mathrm{T}}\,\dot{\boldsymbol{e}}_i + \frac{1}{4}\sum_{i=1}^{N}\sum_{j=1}^{N} g_{ij}\,(\boldsymbol{e}_i - \boldsymbol{e}_j)^{\mathrm{T}}\,(\boldsymbol{e}_i - \boldsymbol{e}_j) + \frac{1}{2}\dot{\boldsymbol{\xi}}^{\mathrm{T}}\left(\widetilde{\mathbb{L}} \otimes \mathbb{I}_3\right)^{-1}(\mathbb{I}_N \otimes \boldsymbol{\Gamma})\,\dot{\boldsymbol{\xi}} \tag{19}$$

where $\otimes$ denotes the Kronecker product, $\boldsymbol{\xi} \triangleq [\boldsymbol{\xi}_1^{\mathrm{T}}, \dots, \boldsymbol{\xi}_N^{\mathrm{T}}]^{\mathrm{T}}$, $\widetilde{\mathbb{L}} \triangleq \kappa\,\mathbb{L} + \mathrm{diag}\,\{\lambda_1^v, \dots, \lambda_N^v\}$, and $\mathbb{I}_N$ is an identity matrix of size N. Since the Laplacian matrix $\mathbb{L}$ is symmetric positive semi-definite, it follows that $\widetilde{\mathbb{L}}$ is symmetric positive definite, and so is $\widetilde{\mathbb{L}}^{-1}$. The derivative of the candidate Lyapunov function V can be written as

$$\dot{V} = \sum_{i=1}^{N} \lambda_i^p\,\dot{\boldsymbol{e}}_i^{\mathrm{T}}\,\boldsymbol{e}_i + \sum_{i=1}^{N} \dot{\boldsymbol{e}}_i^{\mathrm{T}}\left[-\mathbb{C}\,\dot{\boldsymbol{e}}_i - \lambda_i^p\,\boldsymbol{e}_i - \sum_{j=1}^{N} g_{ij}\,(\boldsymbol{e}_i - \boldsymbol{e}_j) - \boldsymbol{\zeta}_i \right] + \frac{1}{2}\sum_{i=1}^{N}\sum_{j=1}^{N} g_{ij}\,(\dot{\boldsymbol{e}}_i - \dot{\boldsymbol{e}}_j)^{\mathrm{T}}\,(\boldsymbol{e}_i - \boldsymbol{e}_j)$$
$$+ \frac{1}{2}\ddot{\boldsymbol{\xi}}^{\mathrm{T}}\left(\widetilde{\mathbb{L}} \otimes \mathbb{I}_3\right)^{-1}(\mathbb{I}_N \otimes \boldsymbol{\Gamma})\,\dot{\boldsymbol{\xi}} + \frac{1}{2}\dot{\boldsymbol{\xi}}^{\mathrm{T}}\left(\widetilde{\mathbb{L}} \otimes \mathbb{I}_3\right)^{-1}(\mathbb{I}_N \otimes \boldsymbol{\Gamma})\,\ddot{\boldsymbol{\xi}} \tag{20}$$

Recalling that $g_{ij} = g_{ji}$, it follows that

$$\sum_{i=1}^{N}\sum_{j=1}^{N} \dot{\boldsymbol{e}}_i^{\mathrm{T}}\,g_{ij}\,(\boldsymbol{e}_i - \boldsymbol{e}_j) = \frac{1}{2}\sum_{i=1}^{N}\sum_{j=1}^{N} \dot{\boldsymbol{e}}_i^{\mathrm{T}}\,g_{ij}\,(\boldsymbol{e}_i - \boldsymbol{e}_j) + \frac{1}{2}\sum_{j=1}^{N}\sum_{i=1}^{N} \dot{\boldsymbol{e}}_j^{\mathrm{T}}\,g_{ji}\,(\boldsymbol{e}_j - \boldsymbol{e}_i)$$
$$= \frac{1}{2}\sum_{i=1}^{N}\sum_{j=1}^{N} g_{ij}\,(\dot{\boldsymbol{e}}_i - \dot{\boldsymbol{e}}_j)^{\mathrm{T}}\,(\boldsymbol{e}_i - \boldsymbol{e}_j) \tag{21}$$

Note that Eq. (16) can be equivalently rewritten in the form

$$\dot{\boldsymbol{\xi}} = (\mathbb{I}_N \otimes \boldsymbol{\Psi})\,\boldsymbol{\xi} + \left(\widetilde{\mathbb{L}} \otimes \mathbb{I}_3\right)\boldsymbol{e} \tag{22}$$

where $\boldsymbol{e} \triangleq [\boldsymbol{e}_1^{\mathrm{T}}, \dots, \boldsymbol{e}_N^{\mathrm{T}}]^{\mathrm{T}}$. Therefore, the time-derivative of V is

$$\dot{V} = -\dot{\boldsymbol{e}}^{\mathrm{T}}(\mathbb{I}_N \otimes \boldsymbol{\Gamma})\,\dot{\boldsymbol{\xi}} + \frac{1}{2}\left[(\mathbb{I}_N \otimes \boldsymbol{\Psi})\,\dot{\boldsymbol{\xi}} + \left(\widetilde{\mathbb{L}} \otimes \mathbb{I}_3\right)\dot{\boldsymbol{e}}\right]^{\mathrm{T}}\left(\widetilde{\mathbb{L}} \otimes \mathbb{I}_3\right)^{-1}(\mathbb{I}_N \otimes \boldsymbol{\Gamma})\,\dot{\boldsymbol{\xi}}$$
$$+ \frac{1}{2}\dot{\boldsymbol{\xi}}^{\mathrm{T}}\left(\widetilde{\mathbb{L}} \otimes \mathbb{I}_3\right)^{-1}(\mathbb{I}_N \otimes \boldsymbol{\Gamma})\left[(\mathbb{I}_N \otimes \boldsymbol{\Psi})\,\dot{\boldsymbol{\xi}} + \left(\widetilde{\mathbb{L}} \otimes \mathbb{I}_3\right)\dot{\boldsymbol{e}}\right]$$
$$= \frac{1}{2}\dot{\boldsymbol{\xi}}^{\mathrm{T}}\left(\widetilde{\mathbb{L}} \otimes \mathbb{I}_3\right)^{-1}[\mathbb{I}_N \otimes (\boldsymbol{\Psi}^{\mathrm{T}}\boldsymbol{\Gamma} + \boldsymbol{\Gamma}\,\boldsymbol{\Psi})]^{\mathrm{T}}\,\dot{\boldsymbol{\xi}}$$
$$= -\frac{1}{2}\dot{\boldsymbol{\xi}}^{\mathrm{T}}\left(\widetilde{\mathbb{L}}^{-1} \otimes \boldsymbol{\Theta}\right)\dot{\boldsymbol{\xi}} \leq 0 \tag{23}$$

Note that $V > 0$ and $\dot{V} \le 0$, therefore $\{e_i, \dot{e}_i, (e_i - e_j), \dot{\xi}\} \in \mathcal{L}_\infty$. Since $\mathbf{\Psi}$ is a Hurwitz matrix, it can be concluded from Eq. (22) that $\ddot{\xi} \in \mathcal{L}_\infty$. It can also be verified that $\ddot{V} \in \mathcal{L}_\infty$ and $\dot{V}$ is uniformly continuous. Using the Barbalat's lemma [25], $\dot{V} \to 0$ as $t \to +\infty$, and hence according to Eq. (23), $\ddot{\xi} \to \mathbf{0}$. From Eq. (22), $\dddot{\xi} \in \mathcal{L}_\infty$, and hence $\ddot{\xi}$ is uniformly continuous. Using the Barbalat's lemma again, $\ddot{\xi} \to \mathbf{0}$. Bearing in mind Eq. (22) and the fact that $\left\{\dot{\xi}, \ddot{\xi}\right\} \to \mathbf{0}$, therefore $\dot{e} \to \mathbf{0}$, which further leads to $\dot{e}_i \to \dot{e}_j \to \mathbf{0}$ by taking the derivative of Eq. (16). From the closed-loop dynamic equation, that is, by substituting Eq. (18) into Eq. (14), it may be also concluded that $e_i \to e_j \to \mathbf{0}$. This completes the proof.

3.2. Adaptive synchronization without mass measurement

For spacecraft equipped with a conventional continuous-thrust propulsion system (as the solar electric thruster), the mass varies with time due to propellant consumption, and often cannot be precisely measured. In that case, it is useful to present an adaptive synchronization algorithm that accounts for mass uncertainties. To proceed, let $\tilde{m}_i$ denote the estimated mass of S_i, and introduce the two auxiliary variables

$$\boldsymbol{\epsilon}_i \triangleq \dot{e}_i + \beta\, e_i, \qquad \boldsymbol{\chi}_i \triangleq \dot{r}_i^\star - \beta\, e_i \tag{24}$$

where $\beta \in \mathbb{R}^+$. Paralleling the approach in Ref. [26], a suitable distributed control law is proposed in the form

$$\boldsymbol{f}_i = \tilde{m}_i\, \boldsymbol{\sigma}_i - \eta_i\, \boldsymbol{\epsilon}_i + \sum_{j=1}^N g_{ij}\, (\boldsymbol{\epsilon}_j - \boldsymbol{\epsilon}_i) \tag{25}$$

where $\eta_i \in \mathbb{R}^+$, and

$$\boldsymbol{\sigma}_i \triangleq \dot{\boldsymbol{\chi}}_i + \mathbb{C}\, \boldsymbol{\chi}_i + \boldsymbol{d}_i \tag{26}$$

Note that Eq. (25) only contains the estimated rather than the actual spacecraft mass information. The updating law for mass estimation $\tilde{m}_i$ is given by

$$\dot{\tilde{m}}_i = -\gamma_i\, \boldsymbol{\epsilon}_i^{\mathrm{T}}\, \boldsymbol{\sigma}_i \tag{27}$$

with $\gamma_i \in \mathbb{R}^+$. Substituting Eqs. (24)–(27) into Eq. (14) yields

$$\dot{\boldsymbol{\epsilon}}_i = -\left(\mathbb{C} + \frac{\eta_i}{m_i}\, \mathbb{I}_3\right) \boldsymbol{\epsilon}_i + \left(\frac{\tilde{m}_i}{m_i} - 1\right) \boldsymbol{\sigma}_i + \frac{1}{m_i} \sum_{j=1}^N g_{ij}\, (\boldsymbol{\epsilon}_j - \boldsymbol{\epsilon}_i) \tag{28}$$

Theorem 2: Using the adaptive control law of Eqs. (24)–(27) for the system described by Eq. (14), synchronized formation tracking is achieved, that is, $e_i \to e_j \to \mathbf{0}$ and $\dot{e}_i \to \dot{e}_j \to \mathbf{0}$ as $t \to +\infty$.

Proof: Consider the candidate Lyapunov function

$$V = \frac{1}{2} \sum_{i=1}^N m_i\, \boldsymbol{\epsilon}_i^{\mathrm{T}}\, \boldsymbol{\epsilon}_i + \frac{1}{2} \sum_{i=1}^N \frac{(\tilde{m}_i - m_i)^2}{\gamma_i} \tag{29}$$

Substituting Eq. (28) into Eq. (29), the time-derivative of V turns out to be

$$\dot{V} = \sum_{i=1}^N \boldsymbol{\epsilon}_i^{\mathrm{T}} \left[-m_i \mathbb{C}\, \boldsymbol{\epsilon}_i - \eta_i\, \boldsymbol{\epsilon}_i + (\tilde{m}_i - m_i)\, \boldsymbol{\sigma}_i + \sum_{j=1}^N g_{ij}\, (\boldsymbol{\epsilon}_j - \boldsymbol{\epsilon}_i) \right] + \sum_{i=1}^N \frac{(\tilde{m}_i - m_i)\, \dot{\tilde{m}}_i}{\gamma_i} \tag{30}$$

Bearing in mind that matrix $\mathbb{C}$ is skew symmetric, and taking into account the equality

$$\sum_{i=1}^N \sum_{j=1}^N g_{ij}\, \boldsymbol{\epsilon}_i^{\mathrm{T}}\, (\boldsymbol{\epsilon}_j - \boldsymbol{\epsilon}_i) = -\frac{1}{2} \sum_{i=1}^N \sum_{j=1}^N g_{ij}\, \|\boldsymbol{\epsilon}_i - \boldsymbol{\epsilon}_j\|^2 \tag{31}$$

Equation (30) can be rewritten in more compact form as

$$\dot{V} = -\sum_{i=1}^N \eta_i\, \|\boldsymbol{\epsilon}_i\|^2 - \frac{1}{2} \sum_{i=1}^N \sum_{j=1}^N g_{ij}\, \|\boldsymbol{\epsilon}_i - \boldsymbol{\epsilon}_j\|^2 \le 0 \tag{32}$$

Paralleling the convergence analysis procedure discussed in the last section, it may be concluded that $e_i \to e_j \to \mathbf{0}$, and $\dot{e}_i \to \dot{e}_j \to \mathbf{0}$.

4. Case study

To illustrate the performance of the proposed distributed adaptive synchronization control laws, a formation mission scenario consisting of three spacecraft around a halo orbit centered at (Sun-Earth system) L_2 point is now discussed. In particular, the three spacecraft in the formation are assumed to have a mass $m_1 \equiv m_2 \equiv m_3 \triangleq 100 \, \text{kg}$. The nominal halo orbit is parameterized using an 8th-order Fourier series, as is discussed before, while the spacecraft trajectories relative to the halo orbit, follow a projected circular orbit with a radius of 10 km.

In the reference frame $\mathcal{T}$, the desired trajectory of spacecraft S_i is given by

$$\boldsymbol{r}_i^\star = \boldsymbol{r}_h + \boldsymbol{\rho}_i^\star, \qquad \dot{\boldsymbol{r}}_i^\star = \dot{\boldsymbol{r}}_h + \dot{\boldsymbol{\rho}}_i^\star \tag{33}$$

where the vectors $\boldsymbol{r}_h$ and $\dot{\boldsymbol{r}}_h$ are obtained from Eqs. (10)–(12), and the algebraic representation of the spacecraft relative orbit is given by

$$\boldsymbol{\rho}_i^\star = [0, \quad 10 \cos{(n_r \, t + \phi_i)}, \quad 10 \sin{(n_r \, t + \phi_i)}]^\mathrm{T} \, \text{km} \tag{34}$$

where the phase angle is $\phi_i = 2 \, (i - 1) \, \pi/3$, and the angular velocity of the relative orbit is $n_r = \omega$. Note that the relative orbit is synchronous (i.e. $n_r = \omega$) with the rotating frame $\mathcal{T}$, otherwise additional propellant consumption would be expected to maintain the relative motion.

The information exchange topology that characterizes the data transmission of the three spacecraft is illustrated in Fig. 4, and the adjacency matrix $\mathbb{G}$ is given by

$$\mathbb{G} = \begin{bmatrix} 0 & 1 & 1 \\ 1 & 0 & 1 \\ 1 & 1 & 0 \end{bmatrix} \tag{35}$$

The initial conditions of the three spacecraft are assumed slightly different from the desired trajectories, with the value of initial errors $\boldsymbol{e}_0 = [e_{x_0}, e_{y_0}, e_{z_0}]^\mathrm{T}$, and $\dot{\boldsymbol{e}}_0 = [\dot{e}_{x_0}, \dot{e}_{y_0}, \dot{e}_{z_0}]^\mathrm{T}$ reassumed in Tab. 2.

4.1. Case without velocity measurement

Consider first the case where the neighbors velocity information is not available. The selection of the control gains is a tradeoff solution between convergence time and propellant consumption. After a trial and error procedure, the set of values to be used in Eqs. (16)–(18) is chosen to be $\lambda_i^p = \lambda_i^v = 10^8$, $\kappa = 10^{-2}$, $\boldsymbol{\Gamma} = 200 \, \mathbb{I}_3$, and $\boldsymbol{\Psi} = -200 \, \mathbb{I}_3$.

The position and velocity errors of the three spacecraft are shown in Figs. 5 and 6, for a time interval of 4 days. The time histories of the intermediate variables $\|\boldsymbol{\xi}_i\|$ are given by Fig. 7, with a random initialization $\boldsymbol{\xi}_{i_0} = \boldsymbol{0}$. The instantaneous relative motion geometry of the formation at $t = \{0, 1, 2\}$ day are illustrated in Fig. 8, in which the stars represent the desired positions of each spacecraft while the circles, squares and diamonds denote their actual positions. It can be clearly seen from the figures that with the control law given by Eqs. (16)–(18), all the spacecraft successfully track the desired projected circular orbit, while synchronization is maintained during transition.

Let $\boldsymbol{u}_i \triangleq \boldsymbol{f}_i/m_i$ denote the propulsive (control) accelerations of S_i, whose components along radial, circumferential and normal directions are shown in Fig. 9. Note that the maximum thrust modulus is on the order of $10^{-3} \, \text{N}$, which is a typical value for an electric propulsion system. The propellant required by each spacecraft for formation keeping can be calculated by integrating the magnitude of the control acceleration as

$$\Delta v_i = \int_0^{t_f} \|\boldsymbol{u}_i\| \, \mathrm{d}t \tag{36}$$

where t_f is the final time. For example, for a mission time of one year, that is, when $t_f = 365.26 \, \text{days}$, the total velocity variations required to maintain the formation are evaluated as $\Delta v_1 = 1.57 \, \text{m/s}$, $\Delta v_2 = 1.57 \, \text{m/s}$, $\Delta v_3 = 1.58 \, \text{m/s}$, respectively. Note that the maximum difference in velocity change among the formation is less than 0.37%, indicating a propellant-balanced formation that is very useful for mission lifetime extension.

Since the nominal halo orbit is parameterized by the Fourier series with a truncated order, a natural question that arises is how much the series order affects the propellant consumption. In order to investigate

this point, the total velocity variation for each spacecraft within one year is reported in Fig. 10, while the series are retained at different orders. As expected, in the presence of the initial errors (see Tab. 2), the propellant required for formation maintenance decreases as the order n of the Fourier series increases. However, this improvement gradually becomes negligible when $n \geq 7$.

4.2. Case of mass uncertainties

Consider now the case in which the spacecraft mass cannot be precisely measured. The control parameters (see Eqs. (24)–(27)) used in the simulation are selected as $\beta = 2.632 \times 10^2$, $\gamma_i = 1$, $\eta_i = 1.316 \times 10^8$, and the initial mass estimation is $\widetilde{m}_{i_0} = 50\,\mathrm{kg}$.

Given the same initial errors as those listed in Tab. 2, the position and velocity errors of the three spacecraft with control law given by Eqs. (24)–(27) are shown in Figs. 11 and 12, for a time interval of $2\,\mathrm{days}$. The relative motion geometry of the formation at $t = \{0, 0.5, 1\}$ day are illustrated in Fig. 13, while the curves of control accelerations are illustrated in Fig. 14. By propagating the orbit for one year, the total amount of velocity variation for each spacecraft is about $\Delta v_1 \simeq \Delta v_2 \simeq \Delta v_3 = 2.14\,\mathrm{m/s}$, while the effect of the Fourier series order of the nominal halo orbit is emphasized in Fig. 15.

Note from Figs. 11–15 that, even in the absence of accurate mass information, all the steady state errors of the three spacecraft still converge to zero (after about one day) while the property of synchronization is maintained along the whole transient motion. Therefore it can be concluded that the control law given by Eqs. (24)–(27) results in a both time-balanced and propellant-balanced formation maneuver.

5. Conclusions

In this paper, the problem of multiple spacecraft formation flying around collinear Lagrange point orbits has been analyzed. A differential correction method has been adopted to obtain the nominal trajectory, while truncated Fourier series have been used to obtain an explicit approximation.

Based on the analytical expression of the nominal trajectory that serves as a reference for formation control design, two distributed adaptive synchronization schemes have been proposed to account for cases in which either a lack of velocity information, or a mass uncertainty exists. In particular, the developed cooperative algorithms rely on a protocol that drives each spacecraft to a desired trajectory, by incorporating every available neighbor-to-neighbor information flow among the formation system so as to reach synchronization in an asymptotic way.

Illustrative examples have shown that the Fourier series-based description is a useful tool for modeling the nominal orbit, and that less control effort is demanded when the series are retained at higher orders. With the inclusion of the shared data couplings among local neighbors, a time-balanced and propellant-balanced formation is guaranteed, and the system robustness is also enhanced.

Acknowledgements

Conflict of interest statement

The authors declared that they have no conflicts of interest to this work.

References

[1] S. Bandyopadhyay, R. Foust, G. P. Subramanian, S.-J. Chung, F. Y. Hadaegh, Review of formation flying and constellation missions using nanosatellites, Journal of Spacecraft and Rockets 53 (3) (2016) 567–578, doi: 10.2514/1.A33291.
[2] K. Alfriend, S. R. Vadali, P. Gurfil, J. How, L. Breger, Spacecraft formation flying: Dynamics, control and navigation, Elsevier, Oxford, 2010, Ch. 1.
[3] E. Gill, O. Montenbruck, S. D'Amico, Autonomous formation flying for the PRISMA mission, Journal of Spacecraft and Rockets 44 (3) (2007) 671–681, doi: 10.2514/1.23015.

[4] C. V. M. Fridlund, F. Capaccioni, Infrared space interferometry – the DARWIN mission, Advances in Space Research 30 (9) (2002) 2135–2145, doi: 10.1016/S0273-1177(02)00585-9.

[5] A. M. Segerman, M. F. Zedd, Preliminary planar formation-flight dynamics near Sun-Earth L_2 point, in: AAS/AIAA Space Flight Mechanics Meeting, AAS-03-133, Ponce, Puerto Rico, 2003.

[6] G. Aliasi, G. Mengali, A. A. Quarta, Artificial lagrange points for solar sail with electrochromic material panels, Journal of Guidance, Control, and Dynamics 36 (5) (2013) 1544–1550, doi: 10.2514/1.58167.

[7] G. Aliasi, G. Mengali, A. A. Quarta, Artificial equilibrium points for a generalized sail in the elliptic restricted three-body problem, Celestial Mechanics and Dynamical Astronomy 114 (1-2) (2012) 181–200, doi: 10.1007/s10569-012-9425-z.

[8] G. Aliasi, G. Mengali, A. A. Quarta, Artificial periodic orbits around L_1-type equilibrium points for a generalized sail, Journal of Guidance, Control, and Dynamics 38 (9) (2015) 1847–1852, doi: 10.2514/1.G000904.

[9] R. W. Farquhar, et al., The flight of isee-3/ice: origins, mission history, and a legacy, Journal of the Astronautical Sciences 49 (1) (2001) 23–73, doi: 10.2514/6.1998-4464.

[10] M. Xu, Y. Liang, X. Fu, Formation flying on quasi-halo orbits in restricted Sun-Earth/Moon system, Aerospace Science and Technology 67 (2017) 118–125, doi: 10.1016/j.ast.2017.03.038.

[11] H. Peng, J. Zhao, Z. Wu, W. Zhong, Optimal periodic controller for formation flying on libration point orbits, Acta Astronautica 69 (7-8) (2011) 537–550, doi: 10.1016/j.actaastro.2011.04.020.

[12] M. Bando, A. Ichikawa, Formation flying along halo orbit of circular-restricted three-body problem, Journal of Guidance, Control, and Dynamics 38 (1) (2015) 123–129, doi: 10.2514/1.G000463.

[13] K. Shahid, K. D. Kumar, Formation control at the Sun-Earth L_2 libration point using solar radiation pressure, Journal of Guidance, Control, and Dynamics 47 (4) (2010) 614–626, doi: 10.2514/1.47342.

[14] A. Héritier, K. C. Howell, Dynamical evolution of natural formations in libration point orbits in a multi-body regime, Acta Astronautica 102 (2014) 332–340, doi: 10.1016/j.actaastro.2013.10.017.

[15] F. J. T. Salazar, O. C. Winter, E. E. Macau, J. J. Masdemont, G. Gomez, Natural formations at the Earth-Moon triangular point in perturbed restricted problems, Advances in Space Research 56 (1) (2015) 144–162, doi: 10.1016/j.asr.2015.03.028.

[16] F. J. T. Salazar, O. C. Winter, E. E. Macau, J. J. Masdemont, G. Gómez, Zero drift regions and control strategies to keep satellite in formation around triangular libration point in the restricted Sun-Earth-Moon scenario, Advances in Space Research 56 (7) (2015) 1502–1518, doi: 10.1016/j.asr.2015.07.001.

[17] D. L. Richardson, Analytic construction of periodic orbits about the collinear points, Celestial Mechanics and Dynamical Astronomy 22 (3) (1980) 241–253, doi: 10.1007/BF01229511.

[18] K. Shahid, K. D. Kumar, Multiple spacecraft formation reconfiguration using solar radiation pressure, Acta Astronautica 103 (2014) 269–281, doi: 10.1016/j.actaastro.2014.05.021.

[19] Y. Akiyama, M. Bando, S. Hokamoto, Station-keeping and formation flying for periodic orbit around Lagrangian points by Fourier series, in: 25th International Symposium on Space Flight Dynamics, Munich, Germany, 2015.

[20] H. Wong, V. Kapila, Spacecraft formation flying near Sun-Earth L_2 Lagrange point: trajectory generation and adaptive output feedback control, in: American Control Conference, IEEE, Portland, OR, USA, 2005, pp. 2411–2418.

[21] D. A. Dei Tos, F. Topputo, Trajectory refinement of three-body orbits in the real solar system model, Advances in Space Research 59 (8) (2017) 2117–2132, doi: 10.1016/j.asr.2017.01.039.

[22] S.-J. Chung, U. Ahsun, J.-J. E. Slotine, Application of synchronization to formation flying spacecraft: Lagrangian approach, Journal of Guidance, Control, and Dynamics 32 (2) (2009) 512–526, doi: 10.2514/1.37261.

[23] D. Spielman, Spectral graph theory, in: U. Naumann, O. Schenk (Eds.), Combinatorial Scientific Computing, Chapman and Hall/CRC, 2012, Ch. 18, pp. 495–500.

[24] W. Ren, Distributed leaderless consensus algorithms for networked Euler-Lagrange systems, International Journal of Control 82 (11) (2009) 2137–2149, doi: 10.1080/00207170902948027.

[25] J. E. Slotine, W. Li, Applied nonlinear control, NJ: Prentice-Hall, New York, 1991, pp. 124–128.

[26] E. Nuno, R. Ortega, L. Basanez, D. Hill, Synchronization of networks of nonidentical Euler-Lagrange systems with uncertain parameters and communication delays, IEEE Transactions on Automatic Control 56 (4) (2011) 935–941, doi: 10.1109/TAC.2010.2103415.

List of Tables

Table 1: Coefficients of the 8th-order Fourier series approximation ($T = 180.36$ days).

i	a_i^c	a_i^s	b_i^c	b_i^s	c_i^c	c_i^s
0	1.0097	0	1.6985×10^{-8}	0	-1.8909×10^{-5}	0
1	-1.4555×10^{-3}	1.0417×10^{-7}	2.4892×10^{-7}	4.5588×10^{-3}	1.1177×10^{-4}	4.8909×10^{-8}
2	1.8093×10^{-4}	-2.0240×10^{-8}	1.1741×10^{-8}	9.5222×10^{-5}	5.9824×10^{-6}	-5.6710×10^{-8}
3	2.2100×10^{-5}	-1.7654×10^{-9}	-1.4157×10^{-9}	2.4015×10^{-5}	9.1473×10^{-7}	1.7828×10^{-8}
4	4.6074×10^{-6}	5.2872×10^{-9}	-5.0973×10^{-9}	4.0751×10^{-6}	1.6450×10^{-7}	2.0573×10^{-9}
5	9.1021×10^{-7}	-6.7798×10^{-9}	1.1295×10^{-9}	8.3572×10^{-7}	2.1952×10^{-8}	4.1663×10^{-9}
6	1.9335×10^{-7}	-6.5334×10^{-9}	-2.2253×10^{-9}	1.4869×10^{-7}	1.9576×10^{-10}	3.2409×10^{-9}
7	3.7976×10^{-8}	-6.5490×10^{-9}	-2.5135×10^{-9}	8.8204×10^{-9}	3.8894×10^{-9}	-1.8873×10^{-9}
8	3.8181×10^{-9}	-6.5361×10^{-9}	-2.5553×10^{-9}	-5.9304×10^{-9}	2.6225×10^{-9}	2.2214×10^{-9}

Table 2: Initial position and velocity errors of three spacecraft.

	e_{x_0} [km]	e_{y_0} [km]	e_{z_0} [km]	$\dot{e}_{x_0}$ [m/s]	$\dot{e}_{y_0}$ [m/s]	$\dot{e}_{z_0}$ [m/s]
S_1	1	-2	2	0	0	0
S_2	2	-2	-1	0	0	0
S_3	-2	2	1	0	0	0

List of Figures

Figure 1: Rotating reference frame in the Sun-Earth CR3BP.
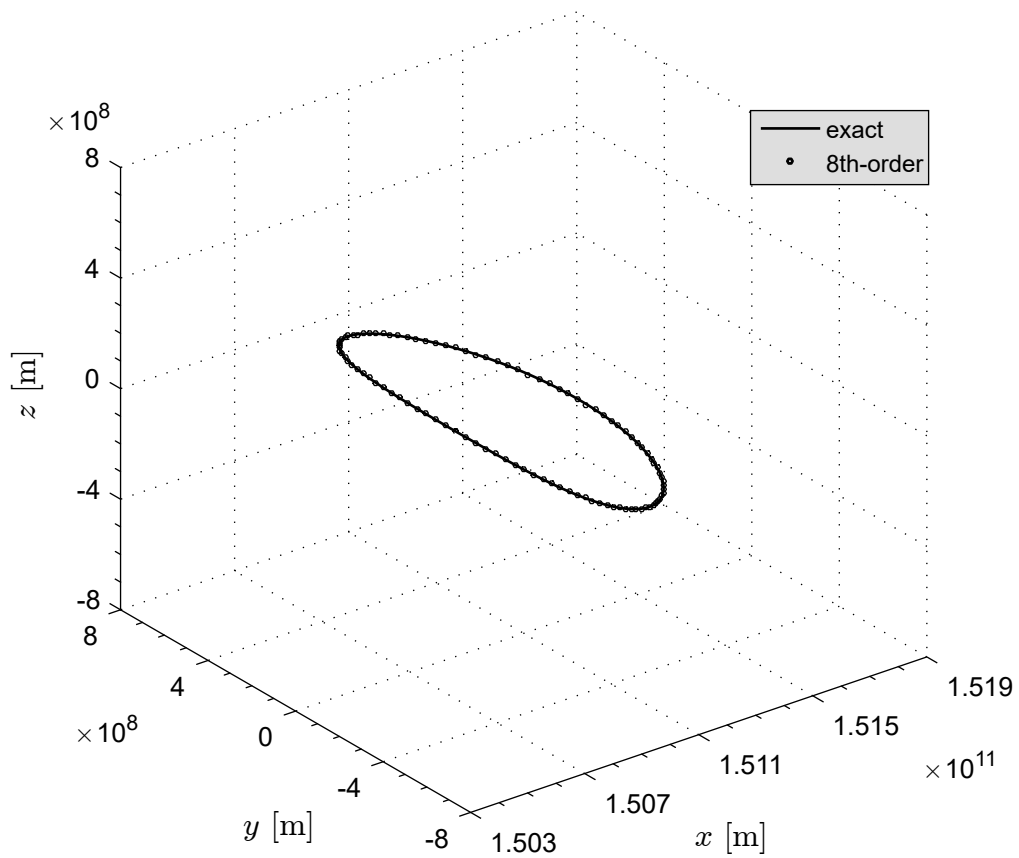
Figure 2: Halo orbit: comparison of the 8th-order Fourier series-based approximation and the exact solution.
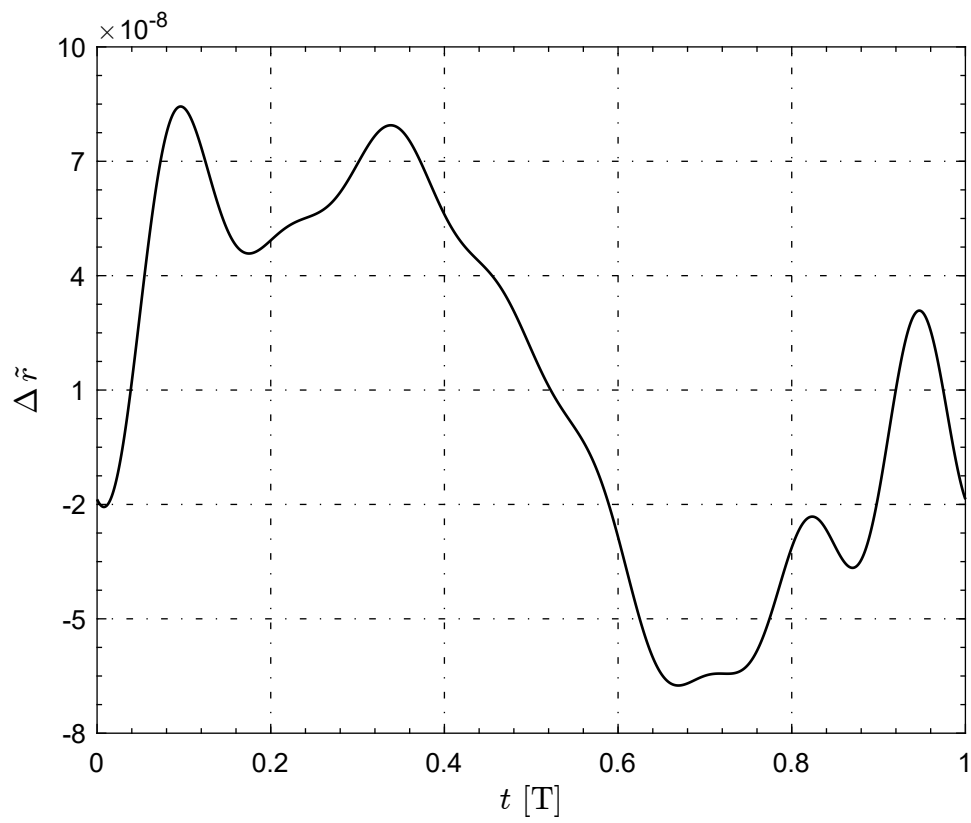
Figure 3: Approximation error of the 8th-order Fourier series-based solution ($T = 180.36$ days).
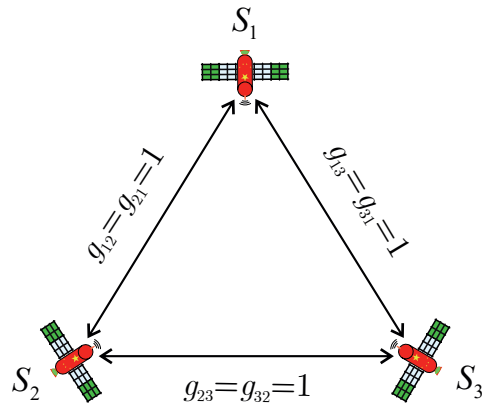
Figure 4: Information exchange topology of the spacecraft formation system.
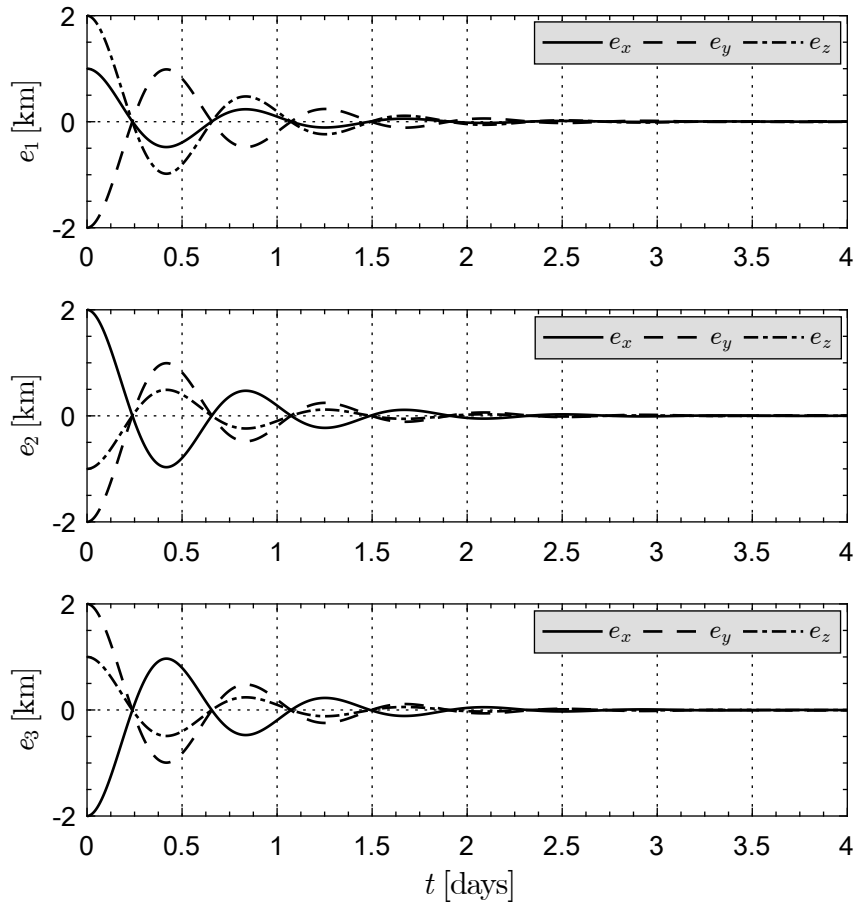
Figure 5: Position errors without velocity measurement.
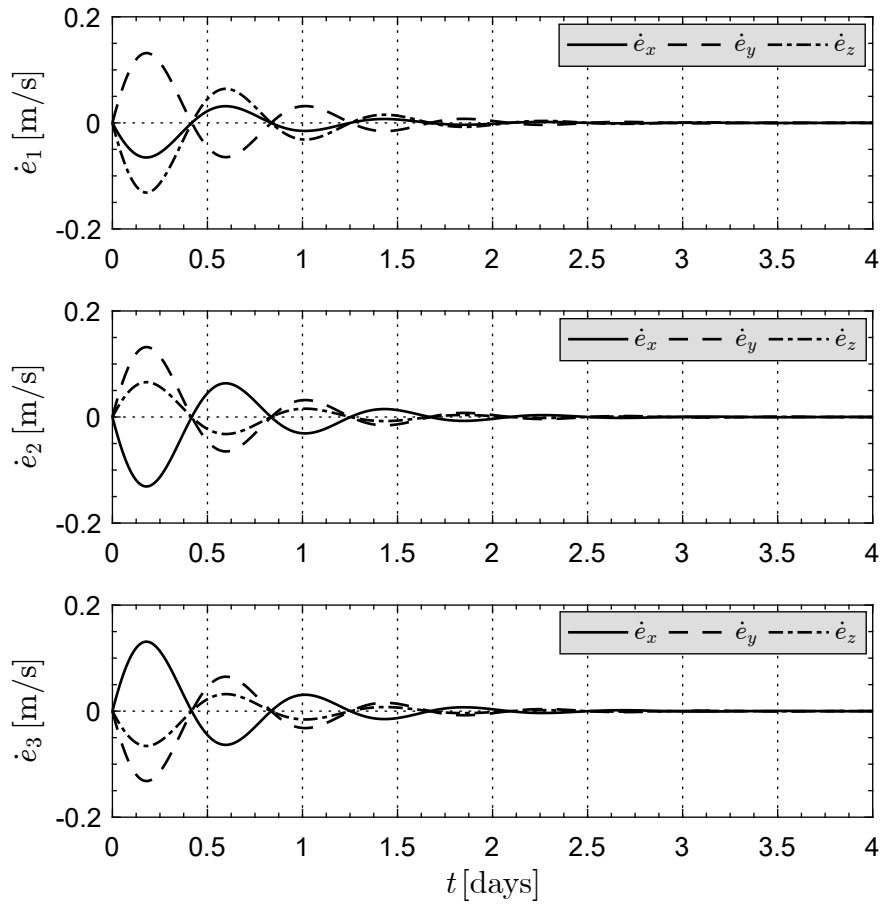
Figure 6: Velocity errors without velocity measurement.
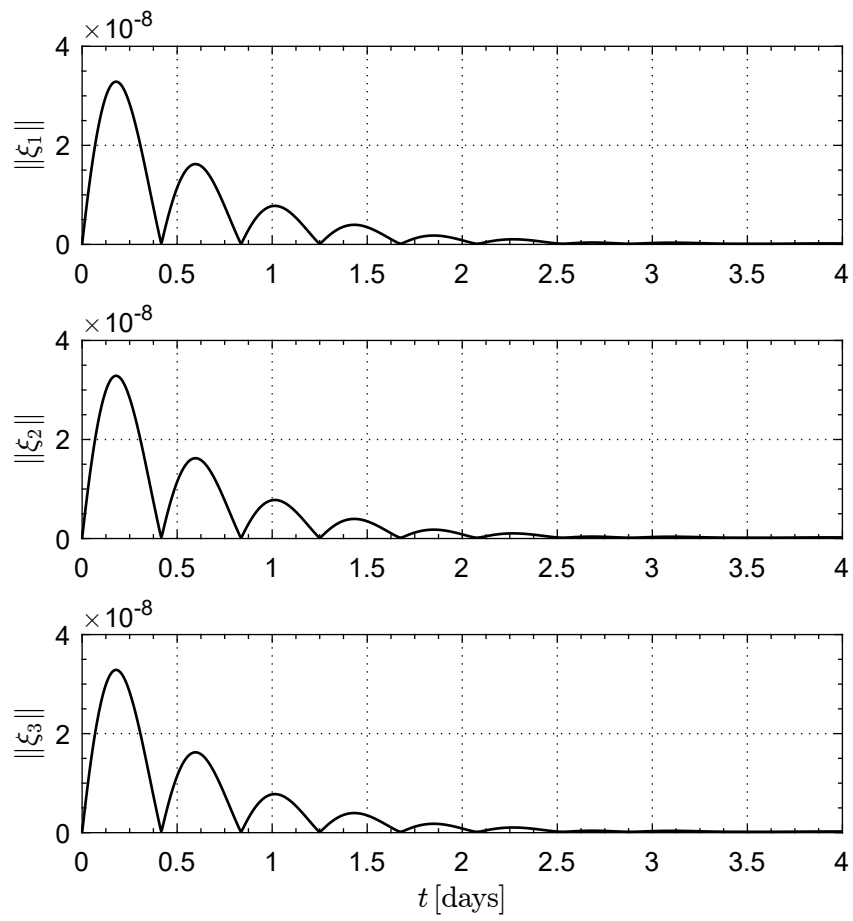
Figure 7: Intermediate variables in Eq. (16).
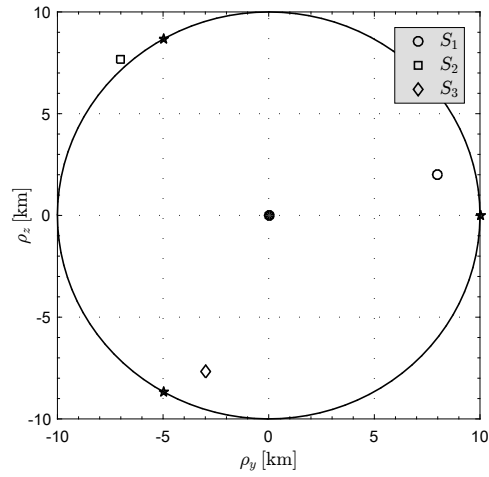
(a) $t = 0$
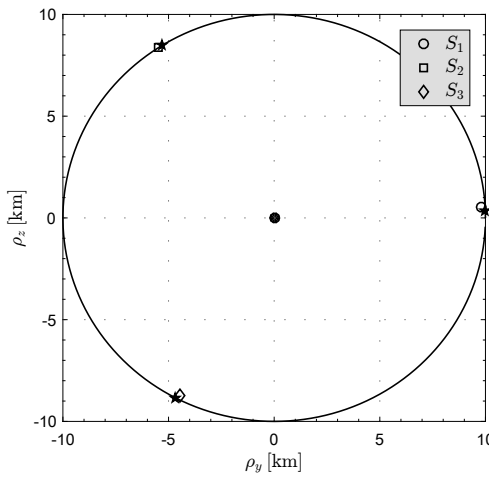
(b) $t = 1 \, \text{day}$
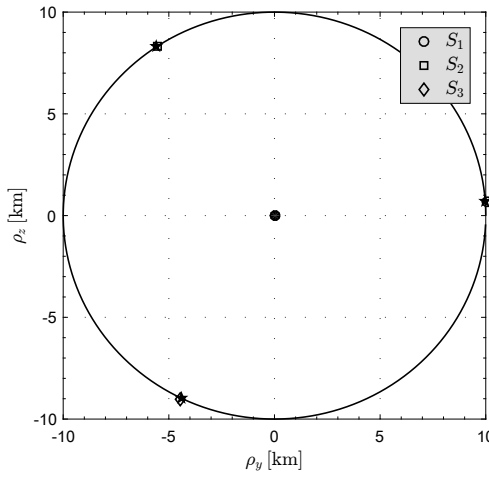
(c) $t = 2 \, \text{days}$

Figure 8: Relative trajectories of the three spacecraft without velocity measurement.

23
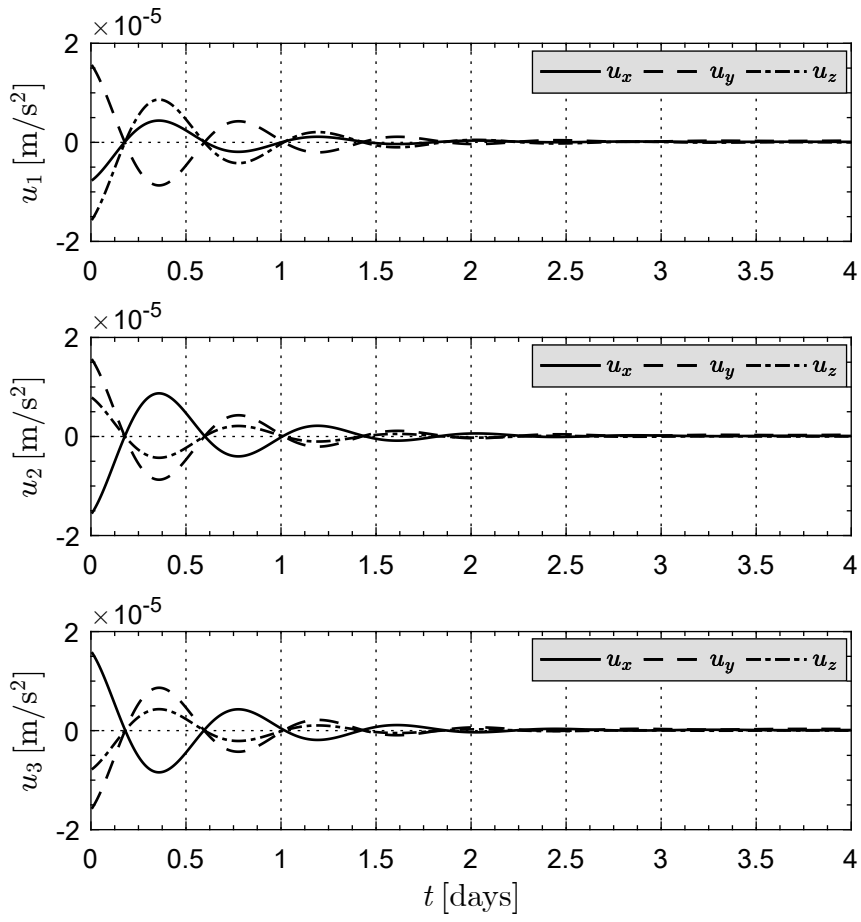
Figure 9: Propulsive (control) accelerations without velocity measurement.
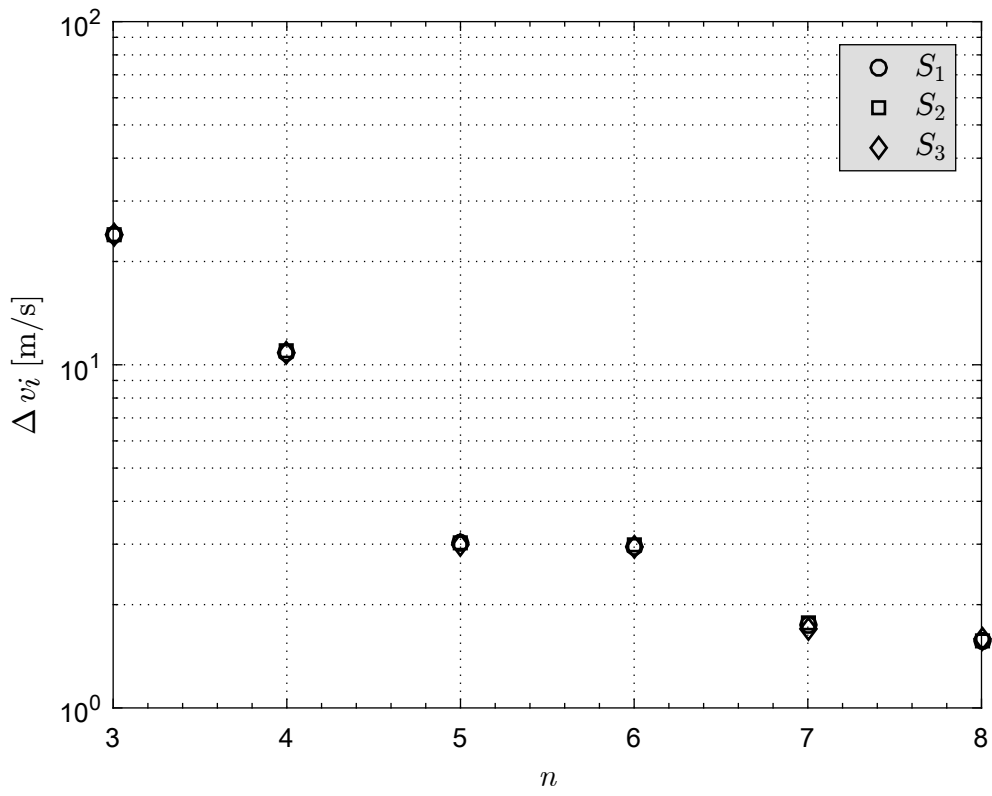
Figure 10: Velocity variations as a function of series order without velocity measurement
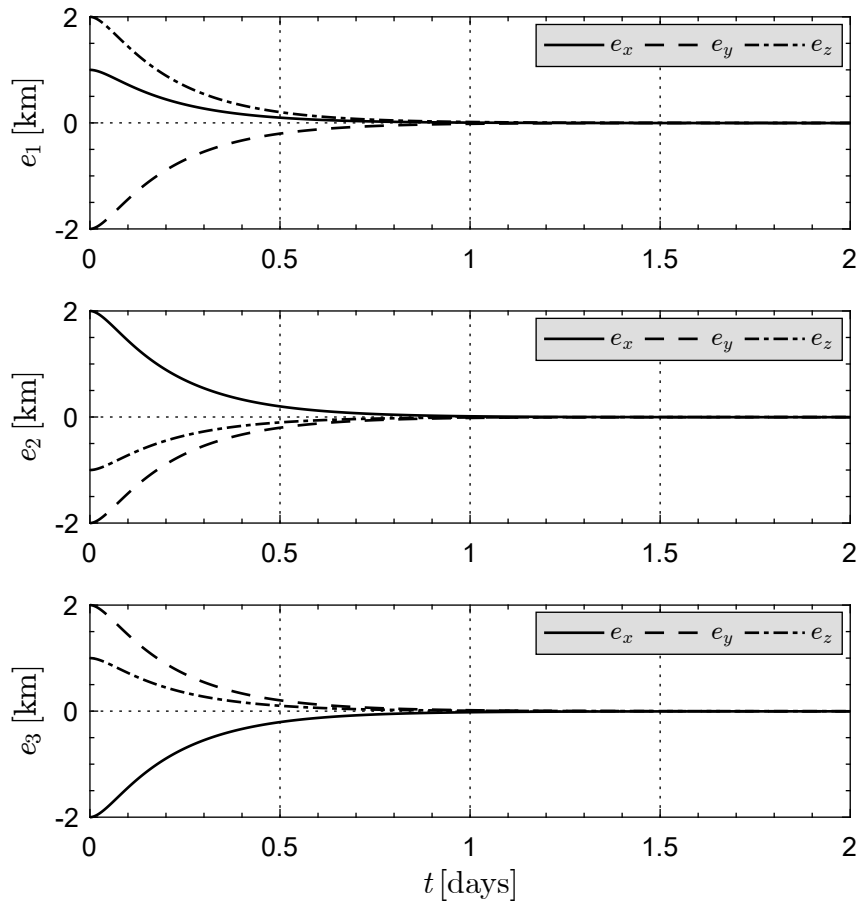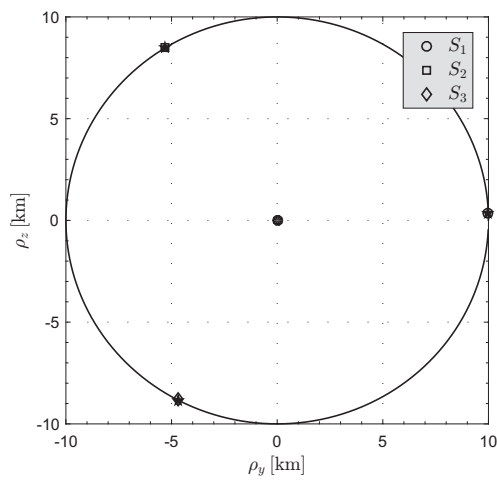
Figure 11: Position errors in the case of mass uncertainties.
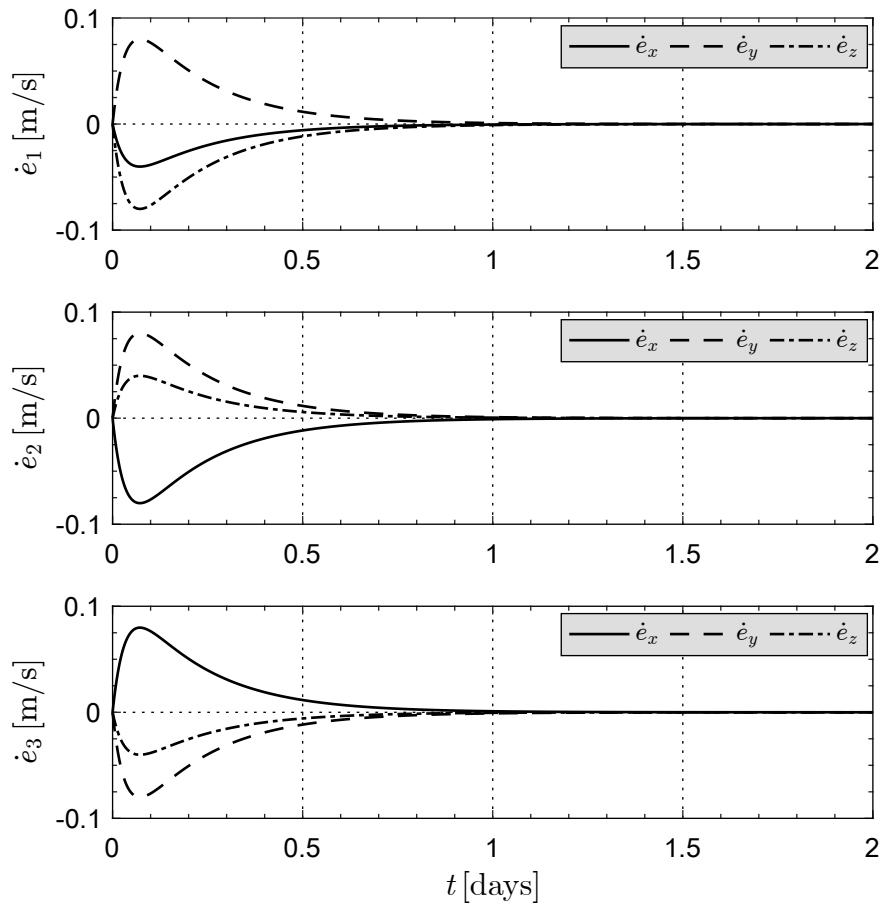
Figure 12: Velocity errors in the case of mass uncertainties.
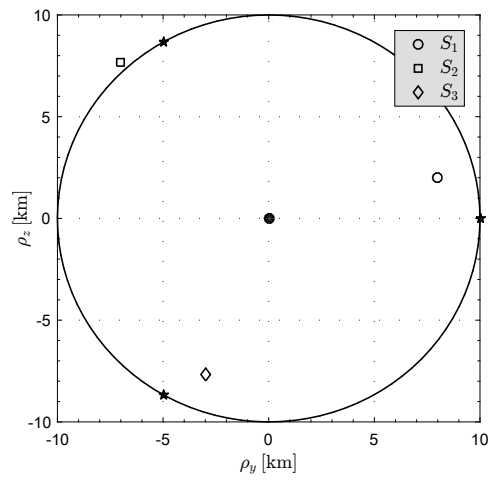
(a) $t = 0$
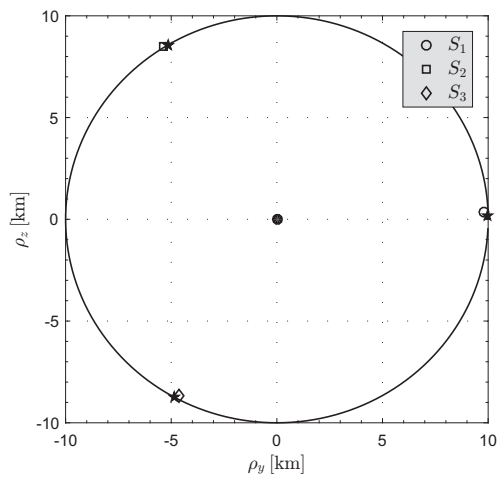
(b) $t = 0.5\,\mathrm{day}$

(c) $t = 1\,\mathrm{day}$

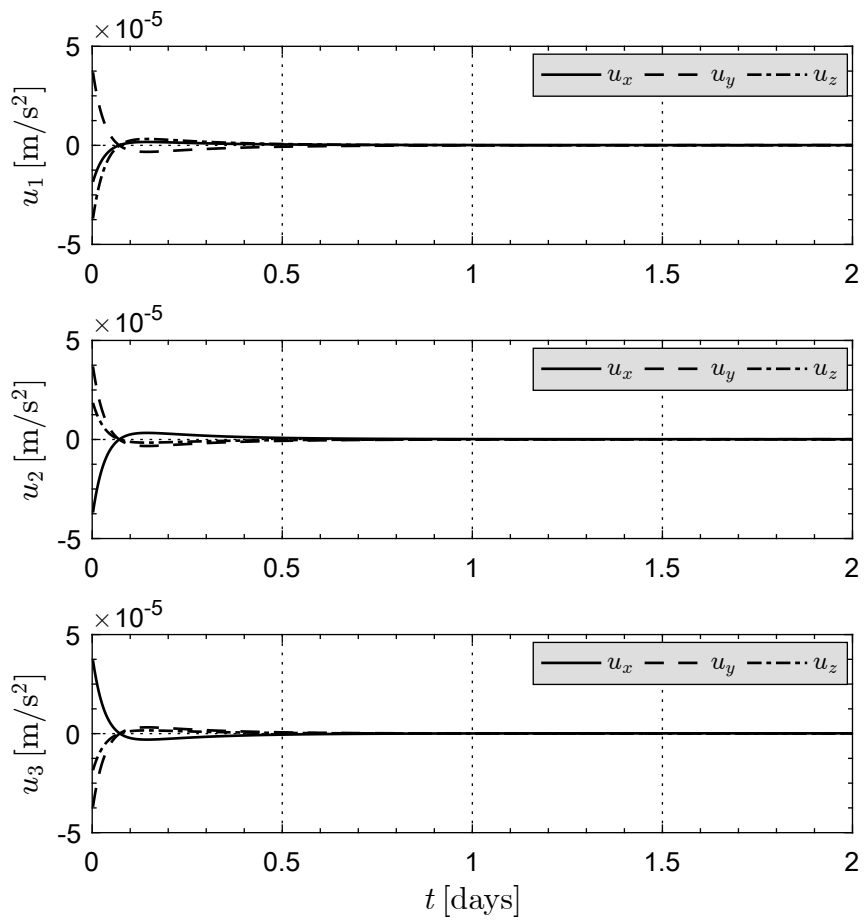Figure 13: Relative trajectories of the three spacecraft in the case of mass uncertainties.

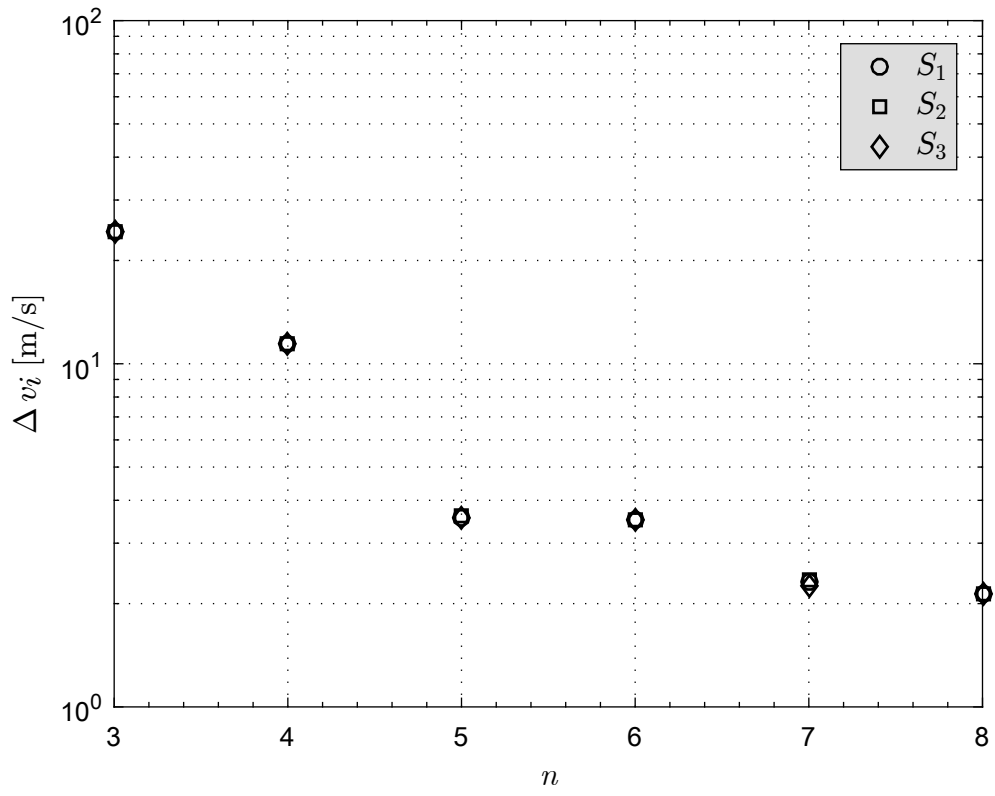Figure 14: Propulsive (control) accelerations in the case of mass uncertainties.

Figure 15: Velocity variations as a function of series order in the case of mass uncertainties.